Comparing Physical and Electrochemical Properties of Different Weave Patterns for Carbon Cloth Electrodes in Redox Flow Batteries

As Published: 10.1115/1.4046661

Publisher: ASME International

Persistent URL: https://hdl.handle.net/1721.1/135241

Version: Final published version: final published article, as it appeared in a journal, conference proceedings, or other formally published context

Comparing Physical and Electrochemical Properties of Different Weave Patterns for Carbon Cloth Electrodes in Redox Flow Batteries

Kevin M. Tenny
Joint Center for Energy Storage Research,
Department of Chemical Engineering,
Massachusetts Institute of Technology,
Cambridge, MA 02139
e-mail: kmtenny@mit.edu

Antoni Forner-Cuenca
Joint Center for Energy Storage Research,
Department of Chemical Engineering,
Massachusetts Institute of Technology,
Cambridge, MA 02139
e-mail: a.forner.cuenca@tue.nl

Yet-Ming Chiang
Joint Center for Energy Storage Research,
Department of Materials Science and Engineering,
Massachusetts Institute of Technology,
Cambridge, MA 02139
e-mail: ychiang@mit.edu

Fikile R. Brushett[1]
Joint Center for Energy Storage Research,
Department of Chemical Engineering,
Massachusetts Institute of Technology,
Cambridge, MA 02139
e-mail: brushett@mit.edu

Redox flow batteries (RFBs) are an emerging electrochemical technology suitable for energy-intensive grid storage, but further cost reductions are needed for broad deployment. Overcoming cell performance limitations through improvements in the design and engineering of constituent components represent a promising pathway to lower system costs. Of particular relevance, but limited in study, are the porous carbon electrodes whose surface composition and microstructure impact multiple aspects of cell behavior. Here, we systematically investigate woven carbon cloth electrodes based on identical carbon fibers but arranged into different weave patterns (plain, 8-harness satin, 2 × 2 basket) of different thicknesses to identify structure–function relations and generalizable descriptors. We first evaluate the physical properties of the electrodes using a suite of analytical methods to quantify structural characteristics, accessible surface area, and permeability. We then study the electrochemical performance in a diagnostic flow cell configuration to elucidate resistive losses through polarization and impedance analysis and to estimate mass transfer coefficients through limiting current measurements. Finally, we combine these findings to develop power law relations between relevant dimensional and dimensionless quantities and to calculate extensive mass transfer coefficients. These studies reveal nuanced relationships between the physical morphology of the electrode and its electrochemical and hydraulic performance and suggest that the plain weave pattern offers the best combination of these attributes. More generally, this study provides physical data and experimental insights that support the development of purpose-built electrodes using a woven materials platform.
[DOI: 10.1115/1.4046661]

Keywords: flow batteries, carbon cloth electrodes, electrochemical storage, mass transfer, electrochemical engineering

1 Introduction

Reconciling the innate variability of renewable resources with consumer and industrial power demands is a key impediment to broad integration of these low-cost electricity generators into the existing grid infrastructure [1,2]. Electrochemical energy storage is viewed as an important enabling technology for facilitating the reliable delivery of electricity from renewables as well as improving grid efficiency through load leveling, arbitrage, and other beneficial services [3]. Redox flow batteries (RFBs) are an emerging option for long-duration energy storage as the separation of power and energy inherent to their architecture enables a range of desirable characteristics including cost-effective scaling [4,5], long operating lifetimes [6], simplified thermal management and maintenance [7–9], and improved safety [10]. Despite this promise, further cost reductions are needed to advance this storage approach including the identification of low-cost, energy dense redox chemistries, and the development of efficient, high-power electrochemical stacks [4,11].

The porous electrode is integral to RFB operation as the material simultaneously: (1) provides active sites for the oxidation and reduction of the active species [12], (2) promotes high species fluxes throughout the media with a minimal hydraulic losses [13,14], (3) supports the facile passage of electrons and heat throughout the phase and across relevant interfaces [12,15], and (4) remains stable in complex electrochemical environments [12]. Consequently, the microstructure and the surface chemistry of these permeable electrodes directly impacts cell power density [16], pumping requirements [17], and performance durability [18], all of which influence system cost [3,7]. To this end, a diverse set of electrodes—typically based on micrometric carbon fibers synthesized from polyacrylonitrile or rayon—have been considered for these applications. These electrodes can be broadly categorized as papers [19–21], felts [16,22,23], and cloths [24–26] based on their method of achieving structural coherence. Recently, our group performed a comparative study of electrodes from all three classes to determine the impact of electrode microstructure on electrochemical performance [27]. We found that with a kinetically facile redox couple, carbon cloth electrodes enable both the highest current density and the lowest pressure drop at a given overpotential and electrolyte velocity.

Cloths are immanently ordered materials consisting of carbon fibers grouped into tows that when threaded together elicit a periodic structure in two spatial dimensions (in-plane) which appears as a weave pattern in the third spatial dimension (through-plane). This fabrication approach can be extended to generate virtually any pattern within certain manufacturing constraints [28], resulting in materials that can exhibit tunable flexibility or durability as compared to their non-woven counterparts [29]. Despite a plethora of comparisons showing the superiority of woven materials to their non-woven counterparts [24–26,29,30], application-specific design of these same materials is limited by a lack of descriptors between weave pattern and electrochemical and hydrodynamic performance.

[1]Corresponding author.

Manuscript received October 1, 2019; final manuscript received March 11, 2020; published online March 12, 2020. Assoc. Editor: Dirk Henkensmeier.

Herein, we systematically investigate the role of weave patterns on the electrochemical performance and the fluid dynamics of carbon cloth electrodes within RFBs. Specifically, we compare four different unactivated carbon cloth electrodes with three different weave patterns (plain, 8-harness satin, 2 × 2 basket) and disparate thicknesses with a goal of identifying structure–function relations and generalizable descriptors. We first evaluate the physical properties of the electrodes using a range of analytical methods to quantify structural characteristics, accessible surface area, and permeability. We then study the electrochemical performance of the electrodes in a diagnostic flow cell configuration to determine limiting currents and to quantify resistive losses. Finally, we combine these findings to develop power law relations between relevant dimensional and dimensionless quantities and to estimate extensive mass transfer coefficients. Ultimately, we aim to provide physical data and experimental insights that support the development of purpose-built electrodes using a woven materials platform.

2 Materials and Methods

2.1 Electrolyte Preparation. The redox couple for this study was 2,2,6,6-tetramethylpiperdin-1-yl)oxyl ($TEMPO^{(\cdot)}$, 98% Sigma Aldrich) and 2,2,6,6-tetramethyl-1-piperdinyloxyo-oxo tetrafluroborate (TEMPO-BF_4; referred to as $TEMPO^{(+)}$). $TEMPO^{(\cdot)}$ was used as-received and the $TEMPO^{(+)}$ was synthesized in an argon glovebox (MBraun Labmaster, $O_2 < 5$ ppm, $H_2O < 1$ ppm) with the oxidizing agent nitrosonium tetrafluoroborate ($NOBF_4$, 98% Alfa Aesar; used as-received) as performed in previous work [27,31]. Tetraethylammonium tetrafluoroborate (TEA-BF_4, 99.99% BASF; used as-received) was used as the supporting salt to increase ionic conductivity and acetonitrile (MeCN, 99.98% BASF) was used as the solvent. A range of different species concentrations were used for the various experiments in this study. The concentrations of the active species, supporting salt, and solvent were 125 mM $TEMPO^{(\cdot)}$ and 125 mM $TEMPO^{(+)}$ with 1 M TEA-BF_4 in MeCN for impedance and polarization; 3 mM $TEMPO^{(\cdot)}$ and 15 mM $TEMPO^{(+)}$ with 1 M TEA-BF_4 in MeCN for limiting current and diffusivity measurements; 1 M TEA-BF_4 in MeCN for electrochemical double-layer capacitance (EDLC); and, MeCN for pressure drop. All solutions were prepared and stored in the glovebox prior to use.

2.2 Electrolyte Characterization. The viscosity of the 50% state-of-charge (SOC) electrolyte was measured for 15 mL samples using a V-700 viscolite vibrational viscometer (±1% reading, Hydramotion) in triplicate to obtain $(3.00 \pm 0.05) \times 10^{-4}$ Pa · s. The diffusion coefficients of $TEMPO^{(\cdot)}$ and $TEMPO^{(+)}$ were estimated from steady-state current measurements of a limiting current electrolyte solution (vide supra) performed on a ca., 11 μm diameter carbon fiber ultramicroelectrode (UME, BASi) [32] using a CH Series 630E potentiostat. A standard three electrode setup was used with the UME as the working electrode, a Pt wire (BASi) counter electrode, and a Li/Li^+ pseudo reference electrode [33] in an argon glovebox. Two cyclic voltammograms were taken per experiment scanning between 3.2 and 3.7 V (versus Li/Li^+) at 10 mV s^{-1}. Three independent experiments were performed.

2.3 Electrode Materials. Four unactivated carbon cloth electrodes (AvCarb Material Solutions, Lowell, MA) were investigated as shown in Fig. 1(*a*) displaying the commercial name and weave type as well as the through-plane and in-plane schematics of each electrode. Note that 1071 HCB and 7497 HCB have the same weave pattern. The 8 × 8 tow grid in Fig. 1(*a*) depicts this structure with the ellipses below and to the right of the schematic signifying the repeated structure of the weave. All four electrodes were based on fibers of the same diameter, 7.5 μm, and other nominal electrode physical properties from the manufacturer [34] are listed in Table 1.

2.4 Physical Characterization. The electrode density was determined by cutting a ca., 2.55 cm^2 area, measuring the electrode thickness, and obtaining the mass of the samples (Mettler Toledo, AB54-S/FACT; ±0.1 mg) for each electrode. The thicknesses of the 1071 HCB, 1698 HCB, and 7497 HCB were measured with a Mitutoyo 7326S caliper (±15 μm), whereas the thicker 1186 HCB was measured with Mitutoyo AOS digimatic absolute caliper (± 0.0254 mm) due to instrument limitations. The measured thickness was also reduced by 30% to estimate the electrode density when under compression in the flow battery. The porosities of the uncompressed and compressed electrodes were determined by Eqs. (1) and (2), respectively

$$\varepsilon = 1 - \frac{\rho_{\text{electrode}}}{\rho_{\text{fiber}}} \tag{1}$$

$$\varepsilon' = 1 - \frac{\rho'_{\text{electrode}}}{\rho_{\text{fiber}}} \tag{2}$$

where ε (−) is the uncompressed porosity, $\rho_{\text{electrode}}$ (kg m^{-3}) is the uncompressed electrode density, and ρ_{fiber} (kg m^{-3}) is the fiber density, $(1.76 \pm 0.01) \times 10^3$ kg m^{-3} per the vendor [34] and is in

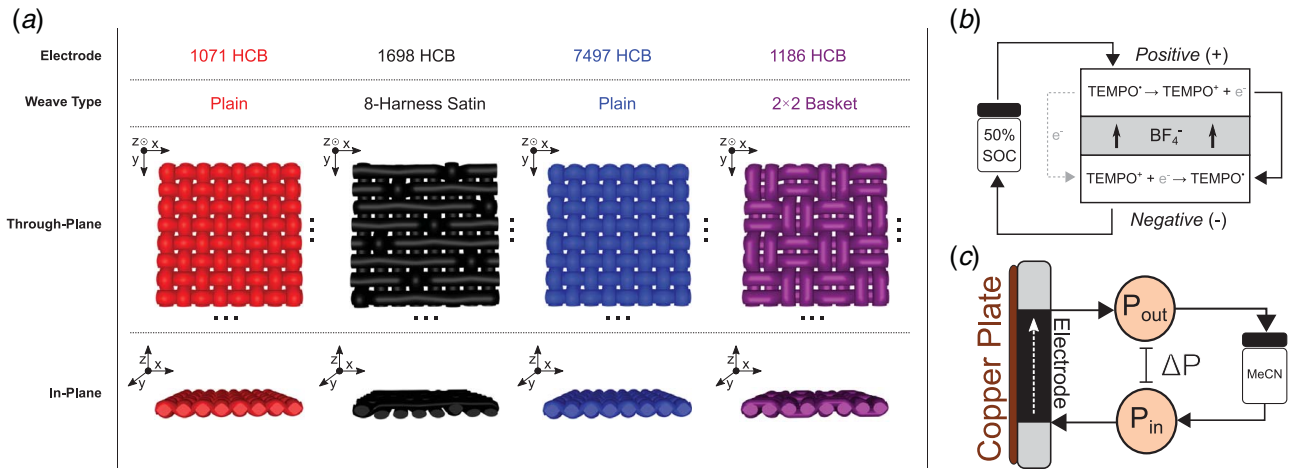

Fig. 1 (*a*) The different weave patterns for each electrode. The ellipses represent the periodic nature of the electrodes. A cross-sectional image of the in-plane directions are shown as this is the direction of the forced advection through the flow field. The weave patterns were generated using TexGen software. (*b*) The single electrolyte cell with a controlled 50% SOC active species concentration. (*c*) The assembly for the in situ electrode pressure drop experiment.

Table 1 Carbon cloth electrode properties with averages calculated with $n = 5$

Commercial name	Weave pattern	Thickness (mm) [34]	Measured thickness (mm)	ε (–)	ε' (–)
1071 HCB	Plain	0.4	0.33 ± 0.00	0.79 ± 0.01	0.70 ± 0.01
1698 HCB	8-Harness satin	0.9	0.76 ± 0.00	0.80 ± 0.01	0.72 ± 0.01
7497 HCB	Plain	0.6	0.61 ± 0.00	0.78 ± 0.01	0.69 ± 0.01
1186 HCB	2 × 2 Basket	1.2	1.64 ± 0.04	0.82 ± 0.01	0.74 ± 0.01

agreement with other carbon fiber density values [35]. The compressed porosity (ε', –) was estimated by using the compressed density value ($\rho'_{\text{electrode}}$, kg m^{-3}). Both ε and ε' are shown in Table 1.

A Zeiss Merlin high-resolution scanning electron microscope (SEM; Zeiss, Germany) was used to image each electrode in the in-plane and through-plane direction. The surface area was mechanically measured through Brunauer-Emmett-Teller (BET) and mercury intrusion porosimetry (MIP). BET was performed by AvCarb Material Solutions with an ASAP 2020 Plus Physisorption (Micrometrics) for nitrogen adsorption and desorption. MIP was performed by Particle Testing Authority (Norcross, GA) with a MicroActive AutoPore V 9600 with a 130.0 deg Hg contact angle and ca., 6.5–6.8 mL penetrometer from 0.1–61,000.0 kPa.

2.5 Electrochemical Performance. The electrochemical performance of the kinetically facile TEMPO$^{(\cdot/+)}$ system was performed in a redox flow battery [31,36] in a single electrolyte cell configuration [37] for SOC control over a range of polarization conditions. A schematic of the single electrolyte assembly is shown in Fig. 1(*b*). The 50% SOC electrolyte solution is pumped from a sealed perfluoroalkyl alkane jar (PFA, 10 mL, Savillex) through PFA tubing (1.6 mm ID, Swagelok). The PFA tubing is connected with a stainless steel union to Masterflex L/S 14 norprene tubing (1.6 mm ID, Cole-Parmer) that enters a flow rate adjustable Easy-Load II peristaltic pump (Cole-Parmer). The electrolyte is then forced into a polypropylene diffuser (Adaptive Engineering Inc.) that is sealed with Kal-rez o-rings (McMaster-Carr). The electrolyte then travels through an in-house machined flow through flow field (FTFF; 3.18 mm, Tokai G347B graphite, MWI, Inc.) of identical dimensions as those reported by Milshtein et al. [19] before coming in contact with the electrode to undergo the electrochemical oxidation of TEMPO$^{(\cdot)}$ and displace an electron. The effluent is then immediately flown to the other side of the diffuser to electrochemically reduce the TEMPO$^{(+)}$ to TEMPO$^{(\cdot)}$ before returning to the reservoir to maintain a nominal 50% SOC. The electrode is abutted between the flow field and a Celgard 2500 (25 μm thick, Fuel Cell Store) separator, where the electrode is compressed to 70% of the nominal thickness with a combination of non-adhesive Gore sealing tape (Gallagher Fluid Seals, Inc.) and polytetrafluoroethylene (McMaster-Carr) that are cut into gaskets.

Given the similar porosity values (Table 1), the variations in the electrode thickness can be accounted for with the superficial velocity as determined by [38]

$$v_s = \frac{Q}{w_e \delta_e} \tag{3}$$

where v_s (m s^{-1}) is the superficial velocity, Q (m^3 s^{-1}) is the volumetric flow rate, w_e (m) is the electrode width, and δ_e (m) is the thickness of the compressed electrode. For all tests in the flow battery, the superficial velocities were 1, 2, 3, 4, and 5 cm s^{-1}. To manage the larger volume flow rates required for the thicker 1186 HCB (>45 mL min^{-1}), a high performance pump head (Model: 77250-62, Cole-Parmer) was used with Masterflex L/S 16HP norprene tubing connected via a stainless steel union to the PFA tubing.

The electrochemical tests were performed in an argon glovebox using a Bio-Logic VMP-3 potentiostat. The single electrolyte cell was run under open circuit voltage (OCV) conditions for 10 min prior to measurement to allow for the electrode wetting. Potentio electrochemical impedance spectroscopy was first performed at OCV in a frequency range of 200 kHz to 10 mHz averaging six points per decade with a sine amplitude of 10 mV. Immediately following, the chronoamperometry measurements were taken by holding the potential for 1 min in steps from 0.0 to 0.6 V in 25 mV increments until the maximum potential or the potentiostat current limit (ca. 400 mA) was reached, whichever occurred first. The final 50% of the data at each potential step was averaged to obtain the polarization data, and the high frequency x-intercept from the Nyquist spectra was used to estimate ohmic losses.

2.6 Pressure Drop. The pressure drop was measured across the electrode as depicted in the schematic in Fig. 1(*c*). For simplicity, only MeCN was used as the measured viscosity of the 50% SOC electrolyte is approximately the same as that of the pure solvent at room temperature (25 °C) [39]. Two pressure gauges (±1% reading; SSI Technologies, Inc.) were placed near the inlet and outlet of the RFB. MeCN was pumped through Masterflex L/S 16 norprene tubing through the inlet pressure gauge, across the electrode, and through the outlet pressure gauge before returning to the reservoir. The cell was allowed to run for 10 min without measurement to ensure electrode wetting. The electrode and the gasket configuration was identical to the electrochemical performance assembly except the electrode was abutted against a copper plate (3 mm thickness, McMaster-Carr) instead of a separator. The same range of superficial velocities (vide supra) were used to measure the pressure drop across the electrode. These measurements were performed in triplicate with near negligible error. In each test, the electrode was removed and the pressure drop was determined for an empty diffuser to account for pressure losses due to the tubing, the fittings, and the reactor volume.

2.7 Electrochemical Double-Layer Capacitance. The EDLC method was performed as one metric to estimate the surface area accessible to electroactive species under flow conditions. While the flow battery architecture remains the same, there are no redox active species in the electrolyte (vide supra) in order to measure the non-Faradaic current contribution. A 10 min OCV hold was employed prior to start to promote wetting and the same set of superficial velocities (vide supra) were used for all EDLC tests. Cyclic voltammograms were taken from −0.3 to 0.3 V at scan rates of 50, 100, 200, 300, and 400 mV s^{-1} with 100% resistance compensation. The positive and negative current values were taken at 0 V to determine the average EDLC current (I_{EDLC}, A) through the following equation:

$$I_{\text{EDLC}} = \frac{1}{2}(I_{\text{ox}} + |I_{\text{red}}|) \tag{4}$$

where I_{ox} (A) is the oxidative current and I_{red} (A) is the reductive current above and below the abscissa, respectively. The EDLC current can then be plotted against the scan rate ($\dot{v}$, V s^{-1}) to determine EDLC capacitance (c_{EDLC}, F) from the slope

$$I_{\text{EDLC}} = c_{\text{EDLC}}\, \dot{v} \tag{5}$$

For all tests, the electrode was removed after the voltammograms to measure the capacitance contributions of the flow fields, connections, etc. This value was subtracted from the in situ electrode value to estimate the EDLC.

The EDLC specific surface area (A_{EDLC}, $m^2\ g^{-1}$) was estimated by using a reference capacitance (c_{ref}, $F\ m^{-1}$) and the electrode mass (m_e, g) through the following:

$$A_{EDLC} = \frac{c_{EDLC}}{c_{ref} m_e} \tag{6}$$

For this study, glassy carbon was used as the reference capacitance and had a value of 1800 $F\ m^{-2}$, as measured with TEA-BF_4 in MeCN [27]. All EDLC measurements were performed twice.

2.8 Limiting Current. The concentration of $TEMPO^{(\cdot)}$ was reduced to 3 mM, as determined via trial-and-error analysis, to enable the system to reach a limiting current value for applied potentials. Prior to chronoamperometric measurements, the cell was held at OCV for 10 min to allow for component wetting. The cell potential was increased in 25 mV increments from 0 V to the final potentials for each electrode: 0.30 V (1071 HCB), 0.45 V (1698 HCB), 0.30 V (7497 HCB), and 0.65 V (1186 HCB). The electrolyte was pumped from the reservoir with MasterFlex L/S 16 norprene tubing with stainless steel unions to the PFA tubing as previously described. For each potential step, the first and the last data points were omitted due to instrument noise; the last 50% of the raw data points were averaged. From this averaged data, the mean of the final three data points at the current plateau were taken as the limiting current value. All limiting current measurements were performed twice.

3 Results and Discussion

We assess the influence of different weave patterns on various morphological and electrochemical properties of a set of carbon cloth electrodes. The morphological characterization of the electrodes is discussed in Sec. 3.1. The measured surface area, polarization, and electrical impedance spectroscopy are detailed in Sec. 3.2. An exploration of the pressure drop and resulting permeability and tortuosity are shown in Sec. 3.3. Finally, the mass transfer coefficient comparison with the pressure drop (Sec. 3.4) and the mass transfer scaling (Sec. 3.5) conclude the analysis.

3.1 Morphological Characterization. Variations in electrode microstructure are expected to impact pressure drop and electrolyte distribution. The first row of Fig. 2 shows the through-plane SEM images of the electrodes, viz., the weave patterns, which provide general insight into the key microstructural features for each cloth. As all the electrodes have a single layer weave, the tow thickness is proportional to the overall cloth thickness. As such, thicker electrodes have bigger tows (1698 HCB, 1186 HCB) comprised of more carbon fibers, whereas thinner electrodes have smaller tows (1071 HCB, 7497 HCB) comprised fewer fibers. While weave patterns illustrated in Fig. 1(*a*) could be visualized for the thinner plain weaves, the 8-harness satin weave of the 1698 HCB and the 2×2 basket weave of the 1186 HCB could not be resolved due to magnification limits of the instrument. However, SEM images do reveal a well-defined through-plane pore of ca., 100 μm between the interwoven tows of all electrodes.

Porosimetry analyses are used to characterize the different pore sizes for each electrode with the MIP plots in the second row of Fig. 2 showing the pore size distribution (PSD) for the four electrodes (assuming cylindrical geometry [40]). All electrodes have a bimodal distribution for pore diameters centered at ca. 10 and 100 μm, with a greater frequency of the larger characteristic pore size. Both the 1071 HCB and 7497 HCB cloths have similar shaped PSDs which is intuitive as both consist of the same weave pattern. The 1698 HCB has the highest frequency of 100 μm pores as the 8-harness satin weave has comparatively infrequent tow overlaps leading to less interlocking and more side-by-side open space. The 2 × 2 basket weave has a broad distribution spanning 10–100 μm, which we attribute to the large tows overlapping two perpendicular tows at a time and create a wider spread in the PSD.

The cross-sectional images reveal the distances between fibers within each tow that are ca. 10 μm and register on the MIP PSD. While the fiber-to-fiber distance will inevitably change under compression, the cylindrical fibers that comprise the tows have been modeled to have high wicking ability [41]; this has the potential

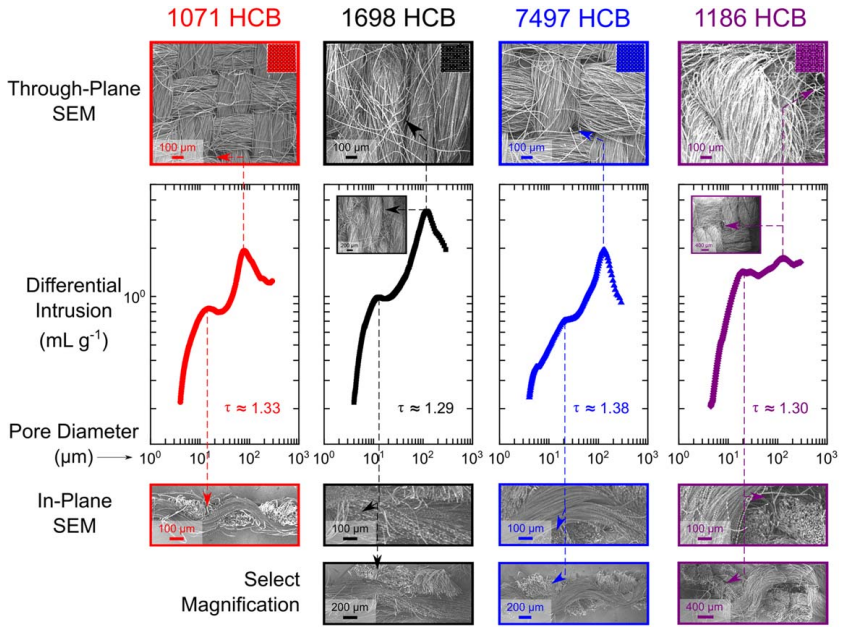

Fig. 2 The MIP plot in the center of the figure outlines the pore size distribution for the four different electrode types. Similarly, all exhibit a bimodal distribution. The first row of SEM images depicts the frontal, through-plane images with the feature sizes of 100 μm and the SEM images on the bottom row show the 10 μm cross-sectional, in-plane images. The values of the MIP graph show the estimated tortuosity values for each electrode.

of diverting flow around the fiber tows. Select magnifications are presented to show the periodicity in the in-plane view. Additionally, the cross-sectional SEM images of the electrodes provide insight into fluid flow during electrochemical operation as the FTFF used in this study promotes near macroscopic, unidirectional flow in-plane. The fiber tow crossings create obstructions to flow that lead to diverted streamlines. The frequency and magnitude of these deviations are anticipated to impact both the pressure drop and the electrochemical performance.

While the differences in the weave patterns are clearly visible, assessment of the hydraulic pathways, which influence pressure drop and permeability of each electrode, is more nuanced. To gain insight, we employ an empirical method developed by Carniglia [42] that uses a cylindrical approximation with measured values such as the total specific intrusion volume by the mercury (V_τ, $m^3\ kg^{-1}$) and the bulk density of the material prior to intrusion (ρ_τ, $kg\ m^{-3}$) to estimate the tortuosity (τ, $-$). For the range of $0.05 \leq (V_\tau \cdot \rho_\tau) \leq 0.95$, the following equation is proposed:

$$\tau = 2.23 - 1.13\, V_\tau \rho_\tau \tag{7}$$

The estimated tortuosity values for each electrode are displayed on the MIP PSD plots in Fig. 2, as the $V_\tau \cdot \rho_\tau$ criteria is satisfied for all cloths (Table S1). The tortuosity estimation in Eq. (7) assumes that the bulk density is the accessible diffusion pathway and that V_τ is the true physical diffusion pathway, thus, the ratio of these two pathways serves as a definition for the tortuosity [43]. Holistically, all the electrodes exhibit similar tortuosity values (1.28–1.35) largely due to the comparable structures (e.g., identical fiber diameters and near-identical porosities). Comparatively, these carbon cloths generally have a lower tortuosity than carbon papers and carbon felts which have been observed to have $\tau > 2$ [29,44] and $\tau > 4$ [45,46], respectively.

In a previous study by El-kharouf et al., the authors obtained different physical properties of carbon cloths, papers, and felts using MIP [29]. Broadly, this study revealed that cloths have lower tortuosities and higher permeabilities as compared with papers and felts. We note that while the MIP PSD and tortuosity values reveal relevant electrode morphological attributes, the experimental conditions differ from those in a flow cell, which may impact accuracy. For example, the maximum foisted pressure during MIP (ca., 60,000 kPa) is several orders of magnitude greater than that of the peristaltic pump (ca., 200 kPa), thus, the "true" hydraulic pathways may not be captured through MIP. In addition, compression of the cloths in the electrochemical cell to reduce ohmic losses [47,48], will deform the electrode, thus impacting pore accessibility; the effect of compression is not considered during MIP. As such, discussions on in situ electrode measurements of permeability and supplemental tortuosity estimations are provided in Sec. 3.3.

3.2 Surface Area, Polarization, and Electrical Impedance Spectroscopy. As the electrode surface area influences the heterogeneous reaction rates, it has been the focus of many research groups [16,18,22,49]. Trasatti and Petrii [50] highlight a variety of methods for measuring physical surface area including BET by measuring gaseous physisorption to the surface [51], MIP that assumes cylindrical pores filled with mercury [40], and EDLC that estimates the non-Faradaic currents to calculate the capacitance of the electrode [52–54]. In addition, depending on the electrode geometry, morphological approximations can be used, such as a large fiber length-to-diameter ratio [21], which assumes a bed of aligned, smooth, and non-overlapping fibers with the carbon fiber length ($\sim O(10^{-2}$ m)) much greater than the fiber diameter, d_f (m) ($\sim O(10^{-6}$ m)), yielding

$$a = \frac{4(1-\varepsilon')}{d_f} \tag{8}$$

The volume-specific surface area, a ($m^2\ m^{-3}$), for each electrode using the four different approaches described above is shown in Fig. 3. The reported EDLC values are an average across all five superficial velocities as there was no statistically significant trend between flow rate and specific capacitance. This indicates that the accessed flow pathways were not altered as function of electrolyte flow rate (Table S2 and Fig. S2, available in the Supplemental Materials on the ASME Digital Collection).

Across the four measurement techniques, there were differences in which electrode had greatest a value. Specifically, for the EDLC and the morphological approximation, the 7497 HCB is observed to have the largest a, whereas for the MIP and the BET measurements, the 1698 HCB showed the largest a. Discrepancies in the ordering of surface areas have been reported in other studies [52,55]; however, the 1186 HCB electrode constantly exhibited the smallest a. A list of the numerical values used in generating Fig. 3 can be found in Table S3 available in the Supplemental Materials on the ASME Digital Collection. Interestingly, the interfacial area values estimated from EDLC are several orders of magnitude lower than those estimated by the other methods. Often, there is less surface area accessible to charged species in solution than the physical surface area [15] due to ion size and solvation states [56,57], which would manifest itself during the EDLC measurements. Nevertheless, the morphological measurement is considered an overestimation [58] in the inherit assumption of long, non-overlapping fibers, and the large discrepancy between EDLC and BET is in agreement with prior reports [59–61]. We were unable to find a direct comparison between EDLC and MIP in the published literature; however, given that BET and MIP are both measured with uncompressed electrodes and have the same order of magnitude values for a, we estimate that the large discrepancy between EDLC and MIP is physically reasonable.

Traditional polarization plots incorporate the extensive current density by normalizing the current with the geometric surface area. While this has use for cell stacking [15], the geometric normalization does not consider the amount of surface area that an electrode has within the cell. Thus, when assessing electrochemical performance, the electrochemical surface area can be used as the intensive variable with which to normalize the current to provide insight into how effective the electrode is at promoting the redox reactions. For example, a conventional iR-corrected polarization curve is shown in Fig. 4(*a*), where the 1071 HCB appears to have a lower electrochemical response as compared with the 1186 HCB. However, when the current is normalized by the surface area measured through EDLC (Fig. 4(*b*)), the 1071 HCB outperforms the 1186 HCB. This normalization considers the effective electrode surface area that is exposed to fluid flow and is available for the redox reaction. Comparatively, this normalization suggests that the 1071 HCB affords better electrochemical performance for

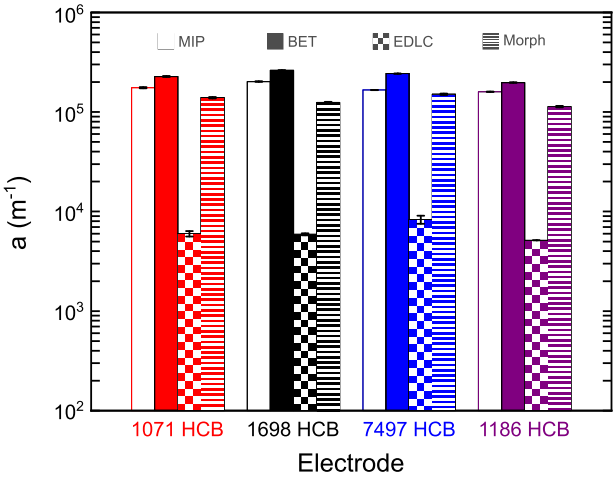

Fig. 3 The volume-specific surface area for the four electrodes as estimated by MIP, BET, EDLC, and morphological methods

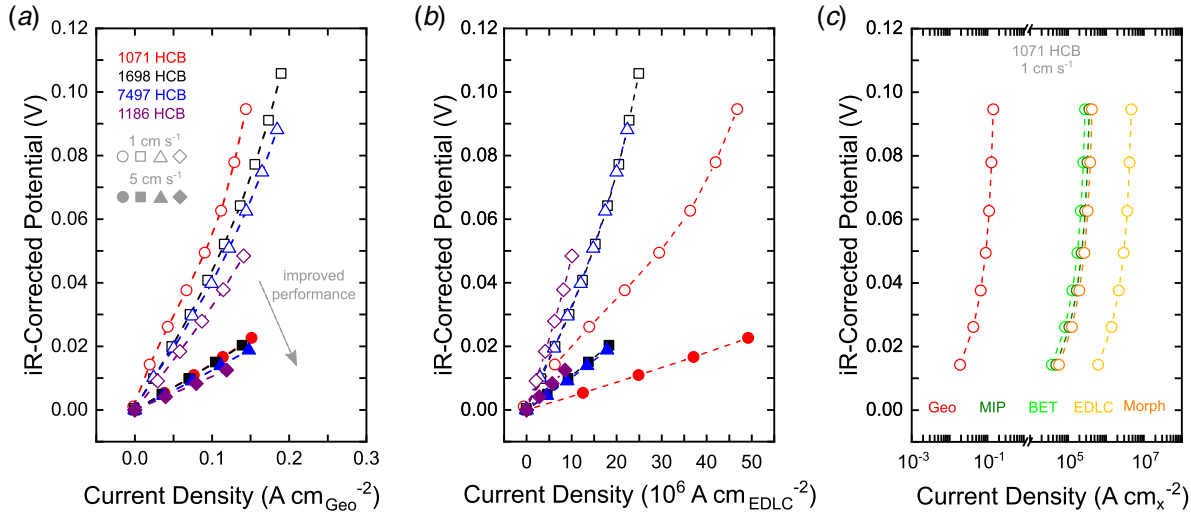

Fig. 4 (*a*) The traditional current density determined by the geometric area for all four electrodes at 1 and 5 cm s^{-1}, (*b*) the current density determined by the measure EDLC surface area displaying a new arrangement of electrode performance, and (c) the current density values for the 1071 HCB electrode at 1 cm s^{-1} for five different surface area measurements with the "*x*" indicating the area-normalization technique

the amount of material in the cell. For probing the effects of electrode structure on the electrochemical response of the system, the polarization plots should extend beyond customary representations for accurate comparison of a matrix of electrodes. Figure 4(*c*) shows the iR-corrected polarization for the 1071 HCB electrode under a 1 cm s^{-1} flowrate for the four surface area measurements in addition to the geometric area. As expected, the shape of the curve does not change; however, the relative current density values vary by multiple orders of magnitude—this is an artifact of the type of surface area imposed for normalization. In choosing any of the supplemental surface area measurements, the order of performance for the four electrodes remains the same (Fig. S3, available in the Supplemental Materials on the ASME Digital Collection).

Electrochemical impedance spectroscopy was performed to determine resistive contributions to cell polarization for each electrode as well as to evaluate if the normalized resistances change with choice in surface area measurement. The Nyquist plots for the four electrodes at 1 and 5 cm s^{-1} are found in Figs. 5(*a*) and 5(*b*), respectively, along with an equivalent circuit fitted to the data by *Z*-weighted frequencies, as previously used in non-aqueous RFBs with porous electrodes [33,62]. This equivalent circuit fitting can afford estimations for the different resistance features due to ohmics, charge transfer, and mass transfer. The fitted parameters for the equivalent circuit for every electrode and electrolyte velocity can be found in the Supplemental Materials (Tables S4–S7); overall, the χ^2 fit was $\sim 10^{-3}$ or less indicating a good fit [63].

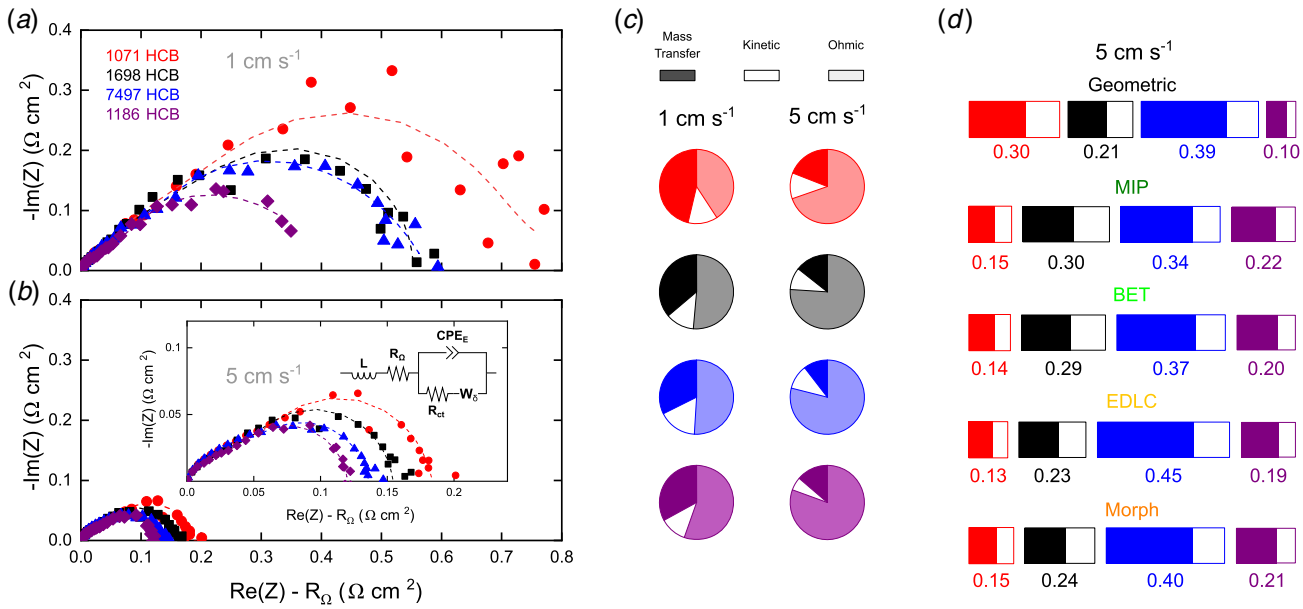

Fig. 5 The geometrically normalized Nyquist plots of the four electrode electrochemical impedance spectroscopy for (*a*) 1 and (*b*) 5 cm s^{-1} fitted to an equivalent circuit. (c) The pie charts showing the relative contributions of the ohmic, charge transfer, and mass transfer resistances from the equivalent circuit. (*d*) The relative normalized resistances (Ω cm^2) at 5 cm s^{-1} for the five common surface area techniques for the four carbon cloth electrodes. The filled bars and the open bars represent the contribution of the mass transfer and the charge transfer, respectively. The ψ_i value (–) for each electrode depicting the normalization of the combined mass and charge transfer resistance for all four electrodes for a given surface area measurement is listed below each bar rounded to two decimal places.

For all electrodes, as the superficial electrolyte velocity increases, the estimated mass transfer resistance sharply decreases and the relative ohmic resistances become the dominant resistance (>50% of total) at higher flow rates (Fig. 5(*c*)). However, the resistance can be normalized through different surface area methods and compared between electrodes through the following equation:

$$\psi_i = \frac{A_{i,k}\sum_j R_j}{\sum_i \left(A_{i,k}\sum_j R_j\right)}, \text{ s.t.} \begin{cases} i \in \{1071, 1698, 7497, 1186\} \\ j \in \{R_{\text{mass transfer}}, R_{\text{charge transfer}}\} \\ k \in \{\text{MIP, BET, EDLC, Morph}\} \end{cases} \quad (9)$$

where ψ_i (−) is the surface area-weighted normalized resistances for the mass transfer and the charge transfer for each electrode (i) and $A_{i,k}$ is the surface area (m^2) selection (k) for each electrode (i). Figure 5(*d*) depicts the ψ_i values for each electrode as normalized by the surface area measurement listed at 5 cm s^{-1}. Interestingly, the 1071 HCB exhibits the lowest mass transfer and charge transfer resistances across all surface area measurements except the geometric. The 7497 HCB electrode, however, is estimated to have the largest relative weighted normalized resistance for the EDLC area measurement. The ψ_i for 1071 HCB is the only value that is consistent with the polarization data in Fig. 5(*b*). Broadly, the order of the ψ_i values among each surface area measurement remains the same despite the surface area measurement. As previously discussed, the 1698 HCB and the 7497 HCB electrodes each had the highest a for the two-of-the-four surface area measurements. In this comparison, the 7497 HCB retains the largest ψ_i, despite the variations in the surface area measurement, suggesting that overall it contains the most charge transfer and mass transfer resistance.

3.3 Pressure Drop, Permeability, and Tortuosity. The hydraulic resistance of the electrode impacts the energy required to achieve a particular fluid flow rate, ultimately contributing to the system energy efficiency [64]. For forced advection across the porous media, Darcy's law [65] is a valuable relationship to determine the permeability (κ, m^2), a compendious, macroscopic property that contains information about the 3D microstructure (i.e., PSD, tortuosity, fiber-to-fiber spacing, etc.). This term is often calculated via the Carman–Kozeny relationship [66] but can also be measured. Using a FTFF with quasi-1D forced advection, the permeability can be assumed to be a scalar value for the unidirectional flow. However, the limitation of using Darcy's law is the implicit assumption of Stokes' flow, specifically that the pressure loss is entirely determined by viscous forces [67]. Instead, Forchheimer [68] proposed an additional term accounting for inertial effects across the porous media to create the Darcy–Forchheimer equation [69] as shown in Eq. (10)

$$\frac{\Delta P}{L} = \underbrace{\frac{\mu}{\kappa} v_s}_{\text{Darcy}} + \underbrace{\beta \rho v_s^2}_{\text{Forchheimer}} \quad (10)$$

where ΔP (Pa) is the pressure drop across the length of the electrode, L (m), μ (Pa · s) is the fluid viscosity, v_s (m s^{-1}) is the superficial fluid velocity, β (m^{-1}) is the Forchheimer factor, and ρ (kg m^{-3}) is the fluid density.

The in situ electrode pressure drop per length of electrode data is shown in Fig. 6(*a*) with a sum of least squares fit to the Darcy–-Forchheimer equation to determine both κ and β. Both the 1071 HCB and the 7497 HCB plain weave patterns elicit the same pressure drop per length suggesting a similar influence of

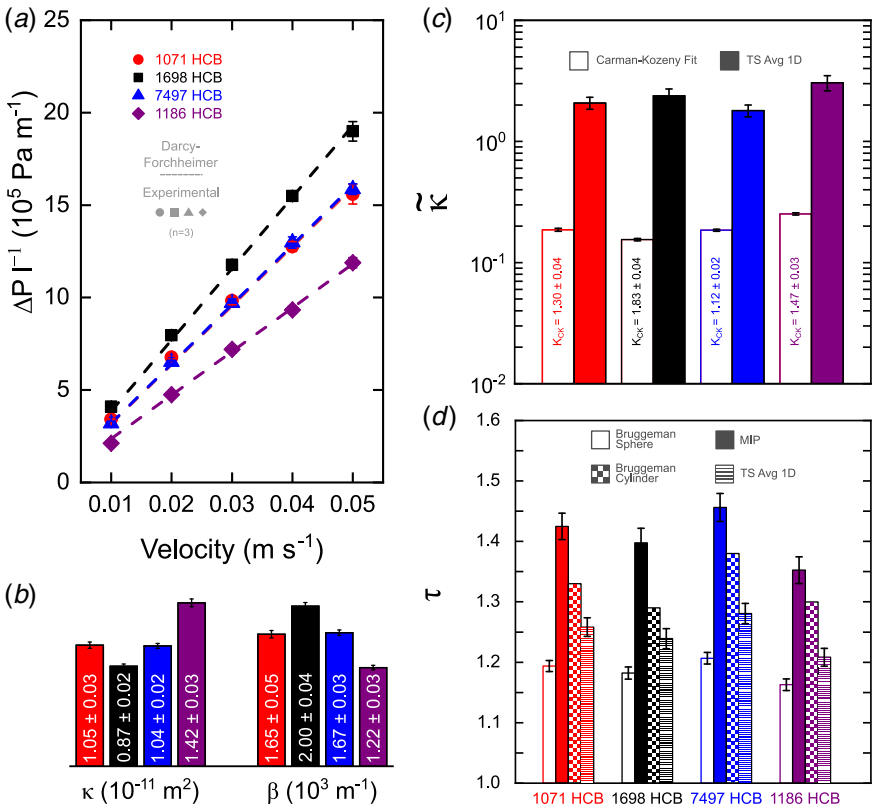

Fig. 6 (*a*) The pressure drop for each superficial velocity for the four different carbon cloth electrodes. The error bars represent triplicate measurements of the in situ electrode experiment fitted to the Darcy–Forchheimer equation; (*b*) the permeability and Forchheimer coefficients for all electrodes; (*c*) the dimensionless permeability of the fitted Carman–Kozeny equation and the TS 1D average permeability; and (*d*) the calculated tortuosity values for the spherical Bruggeman relationship, the cylindrical Bruggeman relationship, the MIP calculated value, and the TS 1D average calculation.

the weave pattern of each electrode on the hydrodynamics. The 1186 HCB electrode has the lowest pressure loss for a given superficial velocity and thus the highest permeability (Fig. 6(*b*)), whereas, conversely, the 1698 HCB electrode had the largest pressure drop and correspondingly the smallest permeability. We hypothesize that the various weave patterns behave differently under compression and can result in changes in the hydraulic permeability. For example, Forner-Cuenca et al. performed a similar study at ca., 15% compression (as opposed to 30%) and found nearly 6× greater permeability ($(6.8 \pm 0.4) \times 10^{-11}$ m^2) for the 1071 HCB cloth [27]. To the best of our knowledge, an explicit relationship between compression and permeability for these cloth materials has yet to be derived and will be the subject of a future publication. We also note that the β values obtained here are lower than those reported in prior literature [27,70–73], suggesting that Darcy flow remains a reasonable approximation in these experiments. An explicit analysis can be found in Sec. 5 available in the Supplemental Materials on the ASME Digital Collection.

The measured permeability values can also be fit to the Carman–Kozeny equation [74,75] shown in Eq. (11) to estimate the Carman–Kozeny coefficient (K_{CK}, –)

$$\kappa = \frac{d_f^2 \varepsilon^3}{16 K_{CK} (1-\varepsilon)^2} \tag{11}$$

The fitting was performed by adjusting K_{CK} to minimize the sum of least squares difference between the dimensionless measured permeability and the dimensionless Carman–Kozeny permeability. The non-dimensional permeability is defined in Eq. (12)

$$\tilde{\kappa} = \frac{\kappa}{d_f^2} \tag{12}$$

The fitted K_{CK} values are shown in Fig. 6(*c*). Generally, K_{CK} values are determined by fitting the permeability values to Eq. (11) over a range of porosity values as the porosity values can change as a result of electrode compression. Hitherto, an exhaustive list of K_{CK}-fitted values for different carbon cloths has not been assembled. However, the K_{CK} value for the plain weave has been previously calculated through pressure drop experiments with compressed air by Gostick et al. for 1D flow at various compressions [70]. Despite material property dissimilarities (e.g., nominal thickness, fiber diameter, porosity, etc.) between the plain weave in that report and in this study, there is statistical overlap between the two experiments (1.446 ± 0.250 [70] compared with 1.30 ± 0.04). While the precise K_{CK} value and statistical range require further enumeration, the two values are reasonably similar despite different advective fluid phases. It is worth noting that the fitted values are lower than reported K_{CK} values for other porous media geometries—a concise but representative list from a literature review can be found in select literature [76].

The woven nature of carbon cloths can result in reduced permeability in the in-plane direction—this is largely due to the hydraulic resistance imposed by the presence of a tow orthogonal to the primary flow direction. As a comparison, another common estimation for permeability was derived by Tomadakis and Sotirchos [77] incorporating multi-dimensional flow through a bed of fibers [78–80]. Known as the Tomadakis–Sotirchos (TS) model, Eq. (13), this relationship can be used for determining the permeability of isotropic and anisotropic materials [70,81]

$$\tilde{\kappa} = \frac{\varepsilon(\varepsilon - \varepsilon_p)^{(\alpha+2)}}{8 \ln(\varepsilon)^2 (1-\varepsilon_p)^{\alpha} (\alpha\, \varepsilon + \varepsilon - \varepsilon_p)^2} \tag{13}$$

where α (–) and ε_p (–) are parameters defined [79] for 1D, 2D, and 3D flow for parallel and normal flow directions. In using Eq. (13), the structure is assumed to be 1D with flow in the parallel and normal directions ($\varepsilon_{p,\parallel} = 0$, $\varepsilon_{p,\perp} = 0.33$, $\alpha_{\parallel}$=0, $\alpha_{\perp} = 0.707$). As shown in Fig. 6(*c*), the TS model permeability is nearly an order of magnitude larger than the Carman-Kozeny-fitted permeability suggesting that solely fiber-based models are not sufficient to capture the effects of the fiber tows, despite their robustness for anisotropy.

The influence of the fiber tows can further impact the tortuosity. Often, the Bruggeman correlation [82,83] is used to determine the tortuosity as shown in Eq. (14) [84]

$$\tau = \frac{1}{\varepsilon^{\xi}}, \quad \text{s.t.} \quad \begin{cases} \xi = 0.5, & \text{spheres} \\ \xi = 1.0, & \text{cylinders} \end{cases} \tag{14}$$

ξ is commonly chosen as 0.5 for determining the tortuosity or extending this relationship to determining effective diffusivity [85,86] or effective conductivity [19,20,86]. However, the Bruggeman correlation is intended for use with isotropic materials and may incur inaccuracies when applied to anisotropic materials [84]. The TS model can also predict the tortuosity (τ, –) [79] via Eq. (15) with greater emphasis on the anisotropy of the material as well as the flow directions

$$\tau = \left(\frac{1-\varepsilon_p}{\varepsilon - \varepsilon_p} \right)^{\alpha} \tag{15}$$

Figure 6(*d*) shows the various τ values for the four electrodes as calculated by the spherical Bruggeman correlation, the cylindrical Bruggeman correlation, MIP, and the 1D TS model. For all four calculations, the 7497 HCB electrode has the largest tortuosity. Interestingly, the 1071 HCB electrode is within statistical overlap with the 7497 HCB electrode for the Bruggeman correlations and the TS model. This aligns with intuition as both electrodes have the same weave pattern.

In considering the possible tortuosity values to use, the base assumptions for each method can be considered. Intuitively, the spherical Bruggeman correlation can be assumed to be the least accurate among all the methods because it contains the least amount of information regarding the fibrous nature. The 1D TS model purports a τ value that can be deduced as less accurate due to the poor fittings of α and ε_p with $\tilde{\kappa}$. The MIP value begins to capture the effect of tortuosity due to the measurement including all the fiber tow dimensions. However, as previously noted, MIP does not incorporate the effect of in operando compression during measurement. Finally, the cylindrical Bruggeman correlation considers the correct fiber geometry and the compressed porosity; however, it does not capture the influence of overlapping fiber tows.

With each τ calculation, key aspects of the morphology are lost. Indeed, a tortuosity measurement under in operando compression and flow conditions would be preferable for determining a veracious value. There are additional numerical approximations for tortuosity using Lattice Boltzmann models [75] and micro-CT images [87]; however, an explicit comparison of these computational techniques is beyond the scope of this work. As an estimation, we elect to use the MIP-determined τ value for subsequent calculations because it incorporates the effect of fiber tows on the structure.

3.4 Mass Transfer Coefficient Comparison. The limiting current experiments were conducted in a single electrolyte flow cell configuration to estimate the mass transfer coefficients for each electrode. This experiment leverages the diminished active species concentration such that at an applied potential the concentration at the electrode surface is assumed to be zero; this manifests itself as a plateau on a polarization curve [88]. Compared with numerical modeling, the limiting current experiment can measure the volume-specific surface area mass transfer coefficient ($a{\cdot}k_m$, s^{-1}) directly. By conducting a control volume analysis and assuming a constant bulk concentration, $a{\cdot}k_m$ can be described as follows in Eq. (16) [89]

$$a \cdot k_m = \frac{I_{\text{lim}}}{n\, F\, C_b\, \delta_e\, w_e\, L} \tag{16}$$

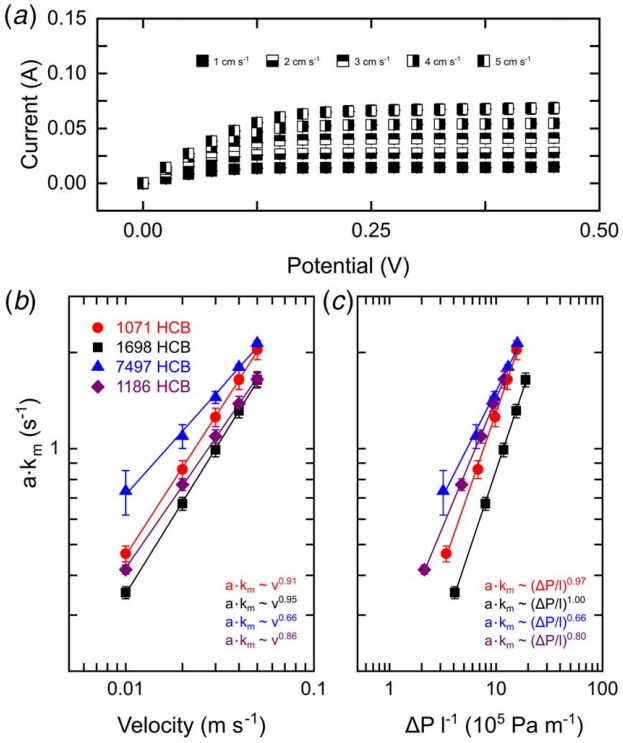

Fig. 7 (*a*) The limiting current plot of the 1698 HCB electrode for various superficial velocities; (*b*) the $a{\cdot}k_m$ values for the different superficial velocities showing the double-log relationship; and (*c*) the $a{\cdot}k_m$ values for different pressure loss per length of electrode to depict the scalability of the mass transfer per pressure requirement

where I_{lim} (A) is the limiting current and n (−) are the number of electrons transferred. The concentrations of the limiting current electrolyte are general asymmetric; the species to be reduced is at a ∼3× higher concentration such that the limiting current is determined by the oxidation reaction [85,90,91]. An example of the limiting current is shown in Fig. 7(*a*) for 1698 HCB with the rest of the limiting current values shown in Fig. S4 available in the Supplemental Materials on the ASME Digital Collection along with the average value in Table S10. Using Eq. (16), the resulting $a{\cdot}k_m$ values for each of the electrodes at the five superficial velocities is found and plotted on a $\log_{10}$–$\log_{10}$, as shown in Fig. 7(*b*), where the slope represents the power law relationship. The $a{\cdot}k_m$ term is shown without assuming a particular surface area measurement; the discussion of the effect of a surface area selection for determining k_m(m s^{-1}) is reserved for Sec. 3.5.

Notably, there is a relatively wide range of the fitted power law values (0.66–0.95) for the four electrodes. Across various electrodes, the specific $a{\cdot}k_m$ value can be difficult to compare as each material has a different amount of a. Table 2 shows the power law relationship for various RFB electrode as determined through the limiting current experiment or a fit to a numerical model with b (−) as the exponential power and γ as the prefactor with units contingent upon the relationship. For each reference in Table 2, the flow through configuration is referenced as the mass transfer coefficient is sensitive to the flow field configuration [19]. The range of fitted power law values for this study (0.65–0.95) fit within the bounds of prior reports on the carbon paper and carbon felt (0.61–1.18) as determined via experimental and computational approaches. The mass transfer coefficients of carbon cloths, felts, and papers appear to have a greater sensitivity to the electrolyte velocity as compared with more niche electrodes, such as the electrospun and the nickel mesh electrodes.

The $a{\cdot}k_m$ values were also compared with the pressure drop for each electrode. As the pressure drop accounts for the length of the electrodes and the quasi-1D forced advection of electrolyte through the electrode, the mass transfer rate appears to be less favorable. This could be a result of the electrode structure that affords regions of preferable mass transfer conditions. The effect of compression on the electrodes is also unknown; however, the in situ electrode pressure drop measurements afford a glimpse into the microstructures of the materials. The mass transfer of the 1071 HCB appears to scale well with the pressure loss across the electrode, which could be beneficial for a multiple stacked electrode [15]. The unity power law relationship for the 1698 HCB suggests that the hydrodynamics that influence the pressure drop concurrently impact the mass transfer. The sub-linear performance for the remainder of the electrodes may be a result of the different hydraulic and mass transfer boundary layer formation; for example, a larger momentum boundary layer compared with a mass transfer boundary layer would allow for increased mass transfer due to the diffusion on slower electrolyte streamlines [67]. Interestingly, as the velocity increases, the $a{\cdot}k_m$ values appear to begin to collapse to a single curve. We hypothesize that this observation is a result of the flow in the electrodes diverting entirely around the fiber tows. Thus, similar weave, such as the periodic, orthogonal tows like the 1071 HCB, the 7497 HCB, and the 1186 HCB, all behave similarly when the hydrodynamics (i.e., pressure drop at equivalent superficial velocities) is considered. The 1698 HCB is the only electrode that forms a diagonal structure (Fig. 1(*a*)), which is not found in the other electrodes.

3.5 Mass Transfer Scaling Analysis. A common engineering extension for mass transfer coefficients is to compute nondimensional numbers such as the Sherwood (Sh) and the Péclet (Pe) number to capture the underlying physics as well as provide a correlation with which to compare with different experimental settings. The Sh defines the relationship between the advective and the

Table 2 Mass transfer relationship for various electrodes

Electrode	Relationship	γ	b	Notes	Ref.
Carbon felt (Hi-Tech, Inc.)	$k_m = \gamma\left(\frac{v}{\varepsilon}\right)^b$	8.85×10^{-4}	0.90	Limiting current	[85]
Carbon felt (Fiber Materials, Inc.)	$\left(\frac{k_m v}{\mathcal{D}}\right) = \gamma\left(\frac{\rho v d_f}{\mu}\right)^b$	1.01	0.61	Limiting current	[89]
Carbon paper (SGL 25AA)	$a\cdot k_m = \gamma\left(\frac{Q}{w_e\delta_e}\right)^b$	0.45	1.18	Numerical fit	[19]
Carbon paper (SGL 29AA)	$\left(\frac{k_m d_f}{\mathcal{D}}\right) = \gamma\left(\frac{v d_f}{\varepsilon\mathcal{D}}\right)^b\left(\frac{\mu}{\rho\mathcal{D}}\right)^{-0.24}$	4.00×10^{-3}	0.75	Numerical fit	[21]
Nickel mesh	$a\cdot k_m = \gamma(v)^b$	8.0×10^{-2}	0.23	Limiting current	[92]
Electrospun	$\left(\frac{k_m d_f}{\mathcal{D}}\right) = \gamma\left(\frac{\rho v d_f}{\mu}\right)^b\left(\frac{\mu}{\rho\mathcal{D}}\right)^{0.432}$	0.906	0.432	Numerical calculation	[93]

Table 3 Length scales for all four carbon cloth electrodes

Porous media length scale (m)	1071 HCB	1698 HCB	7497 HCB	1186 HCB
$(10^6)\cdot d_f$ [34]	7.50	7.50	7.50	7.50
$(10^6)\cdot\sqrt{\kappa}$	3.24 ± 0.52	2.94 ± 0.43	3.23 ± 0.46	3.76 ± 0.58
$(10^8)\cdot\beta\cdot\kappa$	1.73 ± 0.28	1.73 ± 0.25	1.74 ± 0.24	1.74 ± 0.27

diffusive mass transfer and the Pe relates the advective velocity to the diffusive velocity. The equations for Sh and Pe are show in Eqs. (17) and (18), respectively

$$\mathrm{Sh}=\frac{k_m l_c}{\mathcal{D}} \tag{17}$$

$$\mathrm{Pe}=\frac{v l_c}{\mathcal{D}} \tag{18}$$

where k_m (m s^{-1}) is the mass transfer coefficient, l_c (m) is a characteristic length scale, v (m s^{-1}) is a characteristic velocity scale, and $\mathcal{D}$ (m^2 s^{-1}) is the molecular diffusivity.

The diffusivity of TEMPO$^{(\cdot)}$ and TEMPO$^{(+)}$ were determined using an UME. The average of three cyclic voltammograms is shown in the Fig. S1 available in the Supplemental Materials on the ASME Digital Collection. For each of the three trials, fresh limiting current electrolyte solution was used to measure the diffusivity of TEMPO$^{(\cdot)}$ and TEMPO$^{(+)}$. The $\mathcal{D}$ for each were calculated from the established relation [94]

$$\mathcal{D}=\frac{I}{4\,F\,C\,(d/2)} \tag{19}$$

where I (A) is the current, F (96,485 C mol^{-1}) is Faraday's constant, C (mol m^{-1}) is the concentration of each TEMPO species, and d (m) is the UME diameter. The resulting diffusivity of the TEMPO$^{(\cdot)}$ and TEMPO$^{(+)}$ were $(1.46\pm0.14)\times10^{-9}$ and $(1.33\pm0.08)\times10^{-9}$ m^2 s^{-1}, respectively, which are similar to previous work with TEMPO$^{(\cdot/+)}$ [33,95–97]. The TEMPO$^{(+)}$ exhibited a lower diffusivity value due to the interaction with the solvent, as previously seen with oxidized molecules in organic electrolytes [98]. For subsequent calculations involving diffusivity, the average diffusivity of $(1.39\pm0.11)\times10^{-9}$ m^2 s^{-1} is used.

The k_m term is obtained by dividing the $a\cdot k_m$ term from the limiting current method (Eq. (16)) by the volume-specific surface area, a (m^2 m^{-3}). Additionally, Eq. (17) is often adjusted for flow in porous media to account for the changes in the structure of the materials. The effective diffusivity (D_{eff}, m^2 s^{-1}) can also be determined to modify the molecular diffusivity ($\mathcal{D}$, m^2 s^{-1}) to account for the influence of the porous media. The Bruggeman relationship [82] is a ubiquitous method for determining D_{eff} and a recent review on the derivation by Tjaden et al. offer suggestions on its applicability [84]. However, the dispersion coefficient would likely be the most accurate value in promulgating the relationship of diffusivity, porous media structure, and advective flow. For the purposes of this study, we employ a conservative estimation for determining D_{eff} [99].

Using τ from MIP and the compressed porosity, ε', D_{eff} is determined as follows:

$$D_{\mathrm{eff}}=\frac{\mathcal{D}\,\varepsilon'}{\tau} \tag{20}$$

These modifications are then applied to Eqs. (17) and (18) to produce

$$\mathrm{Sh}=\frac{\overbrace{(a\cdot k_m)}^{\text{Limiting current}}\quad\overbrace{l_c}^{\text{Characteristic length}}}{\underbrace{a}_{\text{Surface area technique}}\qquad\underbrace{D_{\mathrm{eff}}}_{\text{Porous media relation}}} \tag{21}$$

$$\mathrm{Pe}=\frac{\overbrace{v}^{\text{Characteristic velocity}}\quad\overbrace{l_c}^{\text{Characteristic length}}}{\underbrace{D_{\mathrm{eff}}}_{\text{Porous media relation}}} \tag{22}$$

Similar to the choice in surface area measurements, the characteristic length, l_c, can vary between porous media. The fiber diameter [21,93], half-powered permeability [67], and $\beta\cdot\kappa$ term [71,100] have been used in the determine dimensionless numbers. These three options are not an exhaustive list of possible scales, as different pore sizes can also be used [101]. However, as the PSD varies under compression, the scope of this study centers on length scales that can be directly measured. The measured characteristic length scales are shown in Table 3.

The half-powered permeability is a similar for all four electrodes which is consistent with the hypothesis that the capillary forces of the fiber tows direct the advection of the electrolyte around the weaves, tangential to the through-plane direction [41]. The explicit derivation for how the half-powered permeability arises from first principles [67]. As discussed in Sec. 3.4, this study operates under Darcy's flow. However, for the purposes of demonstrating various measured lengths scales, the $\beta\cdot\kappa$ term is included, but the reader is cautioned to only consider this metric when in the appropriate flow regime.

Between the four surface area measurements (MIP, BET, EDLC, and long fiber approximation) and the three measured characteristic length scales $\left(d_f,\ \sqrt{\kappa},\ \beta\cdot\kappa\right)$, Eq. (21) can take on twelve relationships. A power law relationship for all relationships can be determined as follows:

$$\mathrm{Sh}=\zeta\,\mathrm{Pe}^{\Theta} \tag{23}$$

where ζ (−) is the prefactor and Θ (−) is the exponential power. An illustration of the different Sh and Pe values for all twelve combinations of surface area and length scale measurements is seen in Fig. 8.

For all electrodes, regardless of the a or l_c choice, the power law relationship remains constant, but the Sh and Pe values can vary by multiple orders of magnitude depending on the selection of l_c and a as reflected in the prefactors (Table S11, available in the Supplemental Materials on the ASME Digital Collection). These differences can influence how the Sh and Pe relationships are understood and compared between chemistries and research groups. For these samples, the quasi-1D forced advection affords an opportunity to obtain an in situ electrode permeability value should K_{CK} for the Carman–Kozeny equation not be known for an electrode and flow field configuration. This value includes microstructural information of the carbon cloths that would serve as an average across the hydraulic pathway of the electrode that are not captured in other physical length scales, such as the fiber diameter. Further, the $a\cdot k_m$ is itself an average across the electrode as obtained by the I_{lim} term from the potentiostat. The D_{eff} term also encompasses averaged information across the entire electrode that account for the variations in the microstructure. Thus, the combination of the parameters matched with a length scale that is averaged across the electrode would be complementary. The permeability-based length scales would be matched with the D_{eff} term to house information about the hydraulic pathways and the effect of microstructure on the performance.

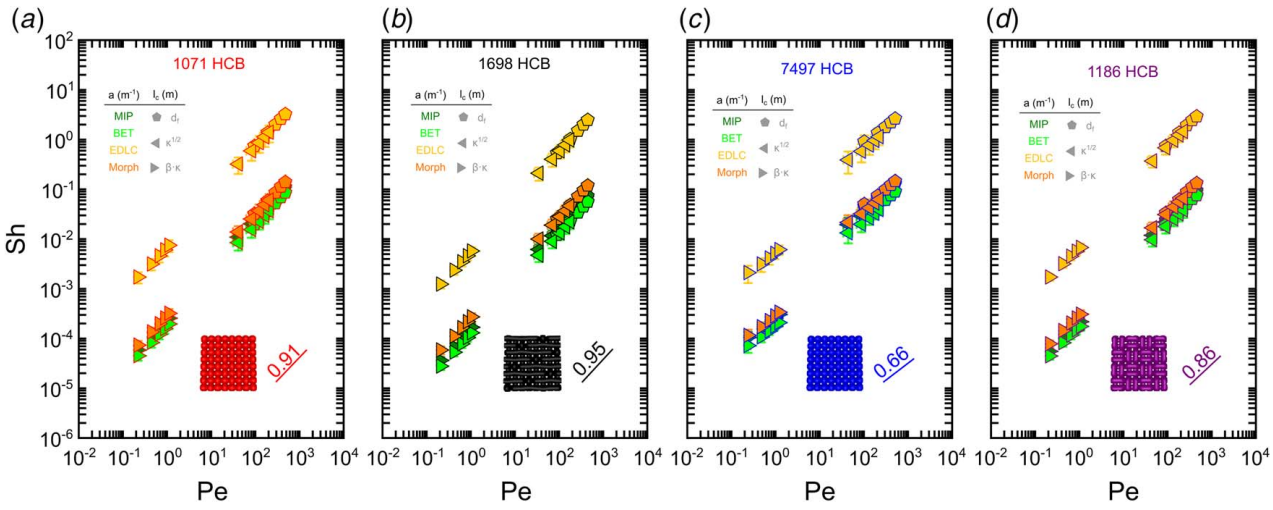

Fig. 8 The Sh as a function of Pe on a $\log_{10}$–$\log_{10}$ scale for the four surface area measurements and the three measurable characteristic length scales. For each *a* and l_c choice, the power law scale stays the same.

4 Conclusions

Flow battery performance is largely influenced by the electrode microstructure, and, in this context, carbon cloths have been identified as a promising candidate. While the flexibility of the manufacturing approach affords a myriad of potential configurations, the impact of the weave pattern on RFB operation remains poorly understood. Using a combination of microscopic, analytical, and electrochemical methods, we assessed electrodes with three different weave patterns, systematically quantifying physical properties and comparing them to performance characteristics in an attempt to elucidate key descriptors. While no weave pattern offered clear advantages across all studied metrics, the analyses provide general insight into how structural characteristics impact electrochemical and hydrodynamic performance. As a specific outcome, we found that with a kinetically facile redox couple in a wetting electrolyte, the 1071 HCB plain weave has the best combination of electrochemical performance, mass transfer overpotential, and pressure drop. In addition, we observed over an order of magnitude deviation in the surface area estimated via electrochemical measurements as compared with physical measurements, which is in agreement with prior reports. While these deviations ultimately did not impact relative assessments of electrode performance and power law correlations, they do affect the absolute magnitude of the dimensionless groups (Sh, Pe), similar to the selection of characteristic length and velocity scales. In comparing our results to the limited set of prior literature, we hypothesize that the compression and associated structural rearrangement of the cloth plays a role in the observed transport behavior and this will be the subject of further studies. Further, while this study provides insight into aggregate electrode properties and performance, determination of spatially defined intra-electrode properties, such as fluid distribution and reaction zones, will likely require in situ flow visualization and velocimetry measurements in combination with microstructure-informed simulations. Continued development of multi-modal characterization methods will further the development of generalizable structure–property relations that may eventually enable chemistry- and flow cell-specific selection and/or design of porous electrodes.

Acknowledgment

We thank AvCarb Material Solutions (Lowell, MA) for providing the electrodes and performing the N_2 BET analyses. We also express gratitude to Katharine V. Greco, McLain E. Leonard, and Michael J. Orella for assistance in manuscript preparation as well as the entirety of the Brushett Research Group for support and helpful suggestions. We further appreciate the invaluable discussions with Professor Emeritus William M. Deen of the Department of Chemical Engineering at MIT.

Funding Data

This work was supported as part of the Joint Center for Energy Storage Research, an Energy Innovation Hub funded by the U.S. Department of Energy, Office of Science, Basic Energy Sciences. K. M. T. acknowledges additional funding from the NSF Graduate Research Fellowship (Grant No. 1122374; Funder ID: 10.13039/100000001), the Tau Beta Pi Graduate Fellowship, and the David H. Koch Chemical Engineering Practice School. A. F.-C. acknowledges a postdoctoral fellowship through the Swiss National Science Foundation (Grant No. PZEZP2_172183; Funder ID: 10.13039/501100001711).

Nomenclature

a = volume-specific surface area, $m^2\ m^{-3}$
b = mass transfer exponential power, –
d = UME diameter, m
f = fractional conversion, –
v_s = superficial velocity, $m\ s^{-1}$
v = characteristic velocity scale, $m\ s^{-1}$
A = surface area, m^2
C = bulk concentration, $mol\ m^{-3}$
F = Faraday's constant, 96,485 $C\ mol^{-1}$
I = current, A ($C\ s^{-1}$)
L = electrode length, m
P = pressure, Pa
Q = volumetric flow rate, $m^3\ s^{-1}$
Pe = Péclet number
Sh = Sherwood number
$\mathcal{D}$ = diffusivity, $m^2\ s^{-1}$
$\dot{v}$ = potential scan rate, $V\ s^{-1}$
c_{EDLC} = non-Faradaic capacitance, F
c_{ref} = reference capacitance, $F\ m^{-2}$
k_m = mass transfer coefficient, $m\ s^{-1}$
l_c = characteristic length scale, m
m_e = electrode mass, g
w_e = electrode width, m
D_{eff} = effective diffusivity, $m^2\ s^{-1}$
I_{EDLC} = EDLC current, A ($C\ s^{-1}$)
I_{lim} = limiting current, A ($C\ s^{-1}$)
I_{ox} = oxidative current, A ($C\ s^{-1}$)
I_{red} = reductive current, A ($C\ s^{-1}$)

K_{CK} = Carman–Kozeny coefficient, –
V_τ = total intrusion specific volume, $m^3\ kg^{-1}$
α = TS model parameter, –
β = Forchheimer factor, m^{-1}
γ = mass transfer prefactor, varies
δ_e = electrode thickness, m
ε = uncompressed porosity, –
ε' = compressed porosity, –
ε_p = TS model parameter, –
ζ = Sh prefactor, –
Θ = Sh exponential power, –
κ = permeability, m^2
$\tilde{\kappa}$ = dimensionless permeability, –
μ = fluid viscosity, Pa · s
ξ = Bruggeman exponent, –
ρ = fluid density, kg m^{-3}
$\rho_{electrode}$ = uncompressed electrode density, kg m^{-3}
$\rho'_{electrode}$ = compressed electrode density, kg m^{-3}
ρ_{fiber} = fiber density, kg m^{-3}
ρ_τ = MIP electrode density, kg m^{-3}
τ = estimated tortuosity, –
ψ_i = fractional normalized weighted resistance, –

References

[1] Chu, S., and Majumdar, A., 2012, "Opportunities and Challenges for a Sustainable Energy Future," Nature, **488**(7411), pp. 294–303.
[2] Ibrahim, H., Ghandour, M., Dimitrova, M., Ilinca, A., and Perron, J., 2011, "Integration of Wind Energy Into Electricity Systems: Technical Challenges and Actual Solutions," Energy Procedia, **6**, pp. 815–824.
[3] Denholm, P., Ela, E., Kirby, B., and Milligan, M., 2010, "The Role of Energy Storage With Renewable Electricity Generation," Technical Report, p. 61.
[4] Resch, M., Bühler, J., Schachler, B., Kunert, R., Meier, A., and Sumper, A., 2019, "Technical and Economic Comparison of Grid Supportive Vanadium Redox Flow Batteries for Primary Control Reserve and Community Electricity Storage in Germany," Int. J. Energy Res., **43**(1), pp. 337–357.
[5] Noack, J., Wietschel, L., Roznyatovskaya, N., Pinkwart, K., and Tübke, J., 2016, "Techno-Economic Modeling and Analysis of Redox Flow Battery Systems," Energies, **9**(8), p. 627.
[6] Li, Z., Pan, M. S., Su, L., Tsai, P.-C., Badel, A. F., Valle, J. M., Eiler, S. L., Xiang, K., Brushett, F. R., and Chiang, Y.-M., 2017, "Air-Breathing Aqueous Sulfur Flow Battery for Ultralow-Cost Long-Duration Electrical Storage," Joule, **1**(2), pp. 306–327.
[7] Weber, A. Z., Mench, M. M., Meyers, J. P., Ross, P. N., Gostick, J. T., and Liu, Q., 2011, "Redox Flow Batteries: A Review," J. Appl. Electrochem., **41**(10), p. 1137–1164.
[8] Wang, W., Luo, Q., Li, B., Wei, X., Li, L., and Yang, Z., 2013, "Recent Progress in Redox Flow Battery Research and Development," Adv. Funct. Mater., **23**(8), pp. 970–986.
[9] Ponce de León, C., Frías-Ferrer, A., González-García, J., Szánto, D. A., and Walsh, F. C., 2006, "Redox Flow Cells for Energy Conversion," J. Power Sources, **160**(1), pp. 716–732.
[10] Whitehead, A. H., Rabbow, T. J., Trampert, M., and Pokorny, P., 2017, "Critical Safety Features of the Vanadium Redox Flow Battery," J. Power Sources, **351**, pp. 1–7.
[11] Lüth, T., König, S., Suriyah, M., and Leibfried, T., 2018, "Passive Components Limit the Cost Reduction of Conventionally Designed Vanadium Redox Flow Batteries," Energy Procedia, **155**, pp. 379–389.
[12] Kim, K. J., Park, M.-S., Kim, Y.-J., Kim, J. H., Dou, S. X., and Skyllas-Kazacos, M., 2015, "A Technology Review of Electrodes and Reaction Mechanisms in Vanadium Redox Flow Batteries," J. Mater. Chem. A, **3**(33), pp. 16913–16933.
[13] Bortolin, S., Toninelli, P., Maggiolo, D., Guarnieri, M., and Col, D. D., 2015, "CFD Study on Electrolyte Distribution in Redox Flow Batteries," J. Phys. Conf. Ser., **655**(1), p. 012049.
[14] Xu, Q., and Zhao, T. S., 2013, "Determination of the Mass-Transport Properties of Vanadium Ions Through the Porous Electrodes of Vanadium Redox Flow Batteries," Phys. Chem. Chem. Phys., **15**(26), p. 10841.
[15] Ke, X., Prahl, J. M., Alexander, J. I. D., Wainright, J. S., Zawodzinski, T. A., and Savinell, R. F., 2018, "Rechargeable Redox Flow Batteries: Flow Fields, Stacks and Design Considerations," Chem. Soc. Rev., **47**(23), pp. 8721–8743.
[16] Sun, B., and Skyllas-Kazacos, M., 1992, "Chemical Modification of Graphite Electrode Materials for Vanadium Redox Flow Battery Application—Part II. Acid Treatments," Electrochim. Acta, **37**(13), pp. 2459–2465.
[17] Tian, C.-H., Chein, R., Hsueh, K.-L., Wu, C.-H., and Tsau, F.-H., 2011, "Design and Modeling of Electrolyte Pumping Power Reduction in Redox Flow Cells," Rare Met., **30**(S1), pp. 16–21.
[18] Greco, K. V., Forner-Cuenca, A., Mularczyk, A., Eller, J., and Brushett, F. R., 2018, "Elucidating the Nuanced Effects of Thermal Pretreatment on Carbon Paper Electrodes for Vanadium Redox Flow Batteries," ACS Appl. Mater. Interfaces, **10**(51), pp. 44430–44442.
[19] Milshtein, J. D., Tenny, K. M., Barton, J. L., Drake, J., Darling, R. M., and Brushett, F. R., 2017, "Quantifying Mass Transfer Rates in Redox Flow Batteries," J. Electrochem. Soc., **164**(11), pp. E3265–E3275.
[20] Gerhardt, M. R., Wong, A. A., and Aziz, M. J., 2018, "The Effect of Interdigitated Channel and Land Dimensions on Flow Cell Performance," J. Electrochem. Soc., **165**(11), pp. A2625–A2643.
[21] Barton, J. L., Milshtein, J. D., Hinricher, J. J., and Brushett, F. R., 2018, "Quantifying the Impact of Viscosity on Mass-Transfer Coefficients in Redox Flow Batteries," J. Power Sources, **399**, pp. 133–143.
[22] Sun, B., and Skyllas-Kazacos, M., 1992, "Modification of Graphite Electrode Materials for Vanadium Redox Flow Battery Application—I. Thermal Treatment," Electrochim. Acta, **37**(7), pp. 1253–1260.
[23] Houser, J., Pezeshki, A., Clement, J. T., Aaron, D., and Mench, M. M., 2017, "Architecture for Improved Mass Transport and System Performance in Redox Flow Batteries," J. Power Sources, **351**, pp. 96–105.
[24] Zhou, X. L., Zhao, T. S., Zeng, Y. K., An, L., and Wei, L., 2016, "A Highly Permeable and Enhanced Surface Area Carbon-Cloth Electrode for Vanadium Redox Flow Batteries," J. Power Sources, **329**, pp. 247–254.
[25] He, Z., Chen, Z., Meng, W., Jiang, Y., Cheng, G., Dai, L., and Wang, L., 2016, "Modified Carbon Cloth as Positive Electrode With High Electrochemical Performance for Vanadium Redox Flow Batteries," J. Energy Chem., **25**(4), pp. 720–725.
[26] Tenny, K. M., Lakhanpal, V. S., Dowd, R. P., Yarlagadda, V., and Van Nguyen, T., 2017, "Impact of Multi-Walled Carbon Nanotube Fabrication on Carbon Cloth Electrodes for Hydrogen-Vanadium Reversible Fuel Cells," J. Electrochem. Soc., **164**(12), pp. A2534–A2538.
[27] Forner-Cuenca, A., Penn, E. E., Oliveira, A. M., and Brushett, F. R., 2019, "Exploring the Role of Electrode Microstructure on the Performance of Non-Aqueous Redox Flow Batteries," J. Electrochem. Soc., **166**(10), pp. A2230–A2241.
[28] Ishmael, N., Fernando, A., Andrew, S., and Taylor, L. W., 2017, "Textile Technologies for the Manufacture of Three-Dimensional Textile Preforms," Res. J. Text. Apparel, **21**(4), pp. 342–362.
[29] El-kharouf, A., Mason, T. J., Brett, D. J. L., and Pollet, B. G., 2012, "Ex-Situ Characterisation of Gas Diffusion Layers for Proton Exchange Membrane Fuel Cells," J. Power Sources, **218**, pp. 393–404.
[30] Jiang, H. R., Zeng, Y. K., Wu, M. C., Shyy, W., and Zhao, T. S., 2019, "A Uniformly Distributed Bismuth Nanoparticle-Modified Carbon Cloth Electrode for Vanadium Redox Flow Batteries," Appl. Energy, **240**, pp. 226–235.
[31] Milshtein, J. D., Kaur, A. P., Casselman, M. D., Kowalski, J. A., Modekrutti, S., Zhang, P. L., Harsha Attanayake, N., Elliott, C. F., Parkin, S. R., Risko, C., Brushett, F. R., and Odom, S. A., 2016, "High Current Density, Long Duration Cycling of Soluble Organic Active Species for Non-Aqueous Redox Flow Batteries," Energy Environ. Sci., **9**(11), pp. 3531–3543.
[32] Su, L., Ferrandon, M., Kowalski, J. A., Vaughey, J. T., and Brushett, F. R., 2014, "Electrolyte Development for Non-Aqueous Redox Flow Batteries Using a High-Throughput Screening Platform," J. Electrochem. Soc., **161**(12), pp. A1905–A1914.
[33] Milshtein, J. D., Barton, J. L., Darling, R. M., and Brushett, F. R., 2016, "4-Acetamido-2,2,6,6-Tetramethylpiperidine-1-Oxyl as a Model Organic Redox Active Compound for Nonaqueous Flow Batteries," J. Power Sources, **327**, pp. 151–159.
[34] AvCarb Material Solutions, https://www.avcarb.com/product-page-fabric/.
[35] Pierson, H. O., 1994, *Handbook of Carbon, Graphite, Diamonds and Fullerenes—Properties, Processing and Applications*, Noyes, New Jersey.
[36] Su, L., Badel, A. F., Cao, C., Hinricher, J. J., and Brushett, F. R., 2017, "Toward an Inexpensive Aqueous Polysulfide–Polyiodide Redox Flow Battery," Ind. Eng. Chem. Res., **56**(35), pp. 9783–9792.
[37] Darling, R. M., and Perry, M. L., 2013, "Pseudo-Steady-State Flow Battery Experiments," ECS Transactions Abstract, **480**.
[38] Darling, R. M., and Perry, M. L., 2014, "The Influence of Electrode and Channel Configurations on Flow Battery Performance," J. Electrochem. Soc., **161**(9), pp. A1381–A1387.
[39] Ritzoulis, G., Papadopoulos, N., and Jannakoudakis, D., 1986, "Densities, Viscosities, and Dielectric Constants of Acetonitrile + Toluene at 15, 25, and 35 .Degree.C," J. Chem. Eng. Data, **31**(2), pp. 146–148.
[40] León y León, C., 1998, "New Perspectives in Mercury Porosimetry," Adv. Colloid Interface Sci., **76**(77), pp. 341–372.
[41] Zhang, Y., Wang, H. P., and Chen, Y. H., 2006, "Capillary Effect of Hydrophobic Polyester Fiber Bundles With Noncircular Cross Section," J. Appl. Polym. Sci., **102**(2), pp. 1405–1412.
[42] Carniglia, S. C., 1986, "Construction of the Tortuosity Factor From Porosimetry," J. Catal., **102**(2), pp. 401–418.
[43] Ghanbarian, B., Hunt, A. G., Ewing, R. P., and Sahimi, M., 2013, "Tortuosity in Porous Media: A Critical Review," Soil Sci. Soc. Am. J., **77**(5), pp. 1461–1477.
[44] Rashapov, R., Imami, F., and Gostick, J. T., 2015, "A Method for Measuring In-Plane Effective Diffusivity in Thin Porous Media," Int. J. Heat Mass Transfer, **85**, pp. 367–374.
[45] Eifert, L., Banerjee, R., Jusys, Z., and Zeis, R., 2018, "Characterization of Carbon Felt Electrodes for Vanadium Redox Flow Batteries: Impact of Treatment Methods," J. Electrochem. Soc., **165**(11), pp. A2577–A2586.
[46] Castañeda, L. F., Walsh, F. C., Nava, J. L., and Ponce de León, C., 2017, "Graphite Felt as a Versatile Electrode Material: Properties, Reaction Environment, Performance and Applications," Electrochim. Acta, **258**, pp. 1115–1139.
[47] Pezeshki, A. M., Clement, J. T., Veith, G. M., Zawodzinski, T. A., and Mench, M. M., 2015, "High Performance Electrodes in Vanadium Redox Flow Batteries

Through Oxygen-Enriched Thermal Activation," J. Power Sources, **294**, pp. 333–338.
[48] Park, S.-K., Shim, J., Yang, J. H., Jin, C.-S., Lee, B. S., Lee, Y.-S., Shin, K.-H., and Jeon, J.-D., 2014, "The Influence of Compressed Carbon Felt Electrodes on the Performance of a Vanadium Redox Flow Battery," Electrochim. Acta, **116**, pp. 447–452.
[49] Schneider, J., Bulczak, E., El-Nagar, G. A., Gebhard, M., Kubella, P., Schnucklake, M., Fetyan, A., Derr, I., and Roth, C., 2019, "Degradation Phenomena of Bismuth-Modified Felt Electrodes in VRFB Studied by Electrochemical Impedance Spectroscopy," Batteries, **5**(1), p. 16.
[50] Trasatti, S., and Petrii, O. A., 1992, "Real Surface Area Measurements in Electrochemistry," J. Electroanal. Chem., **327**(1), pp. 353–376.
[51] Naderi, M., 2015, "Chapter Fourteen—Surface Area: Brunauer–Emmett–Teller (BET)," *Progress in Filtration and Separation*, S. Tarleton, ed., Academic Press, Oxford, pp. 585–608.
[52] Han, L., Karthikeyan, K. G., Anderson, M. A., and Gregory, K. B., 2014, "Exploring the Impact of Pore Size Distribution on the Performance of Carbon Electrodes for Capacitive Deionization," J. Colloid Interface Sci., **430**, pp. 93–99.
[53] Hahn, M., Kötz, R., Gallay, R., and Siggel, A., 2006, "Pressure Evolution in Propylene Carbonate Based Electrochemical Double Layer Capacitors," Electrochim. Acta, **52**(4), pp. 1709–1712.
[54] Urita, K., Urita, C., Fujita, K., Horio, K., Yoshida, M., and Moriguchi, I., 2017, "The Ideal Porous Structure of EDLC Carbon Electrodes With Extremely High Capacitance," Nanoscale, **9**(40), pp. 15643–15649.
[55] Zhao, Y., Zhao, Z., Zhang, J., Wei, M., Xiao, L., and Hou, L., 2018, "Distinctive Performance of Gemini Surfactant in the Preparation of Hierarchically Porous Carbons via High-Internal-Phase Emulsion Template," Langmuir, **34**(40), pp. 12100–12108.
[56] Endo, M., Maeda, T., Takeda, T., Kim, Y. J., Koshiba, K., Hara, H., and Dresselhaus, M. S., 2001, "Capacitance and Pore-Size Distribution in Aqueous and Nonaqueous Electrolytes Using Various Activated Carbon Electrodes," J. Electrochem. Soc., **148**(8), p. A910.
[57] Koh, A. R., Hwang, B., Roh, K. C., and Kim, K., 2014, "The Effect of the Ionic Size of Small Quaternary Ammonium BF4 Salts on Electrochemical Double Layer Capacitors," Phys. Chem. Chem. Phys., **16**(29), pp. 15146–15151.
[58] Kok, M. D. R., Khalifa, A., and Gostick, J. T., 2016, "Multiphysics Simulation of the Flow Battery Cathode: Cell Architecture and Electrode Optimization," J. Electrochem. Soc., **163**(7), pp. A1408–A1419.
[59] Mosch, H. L. K. S., Akintola, O., Plass, W., Höppener, S., Schubert, U. S., and Ignaszak, A., 2016, "Specific Surface Versus Electrochemically Active Area of the Carbon/Polypyrrole Capacitor: Correlation of Ion Dynamics Studied by an Electrochemical Quartz Crystal Microbalance With BET Surface," Langmuir, **32**(18), pp. 4440–4449.
[60] Jung, S., McCrory, C. C. L., Ferrer, I. M., Peters, J. C., and Jaramillo, T. F., 2016, "Benchmarking Nanoparticulate Metal Oxide Electrocatalysts for the Alkaline Water Oxidation Reaction," J. Mater. Chem. A, **4**(8), pp. 3068–3076.
[61] Holze, R., and Vielstich, W., 1984, "Double-Layer Capacity Measurements as a Method to Characterize Porous Fuel Cell Electrodes," Electrochim. Acta, **29**(5), pp. 607–610.
[62] Escalante-García, I. L., Wainright, J. S., Thompson, L. T., and Savinell, R. F., 2015, "Performance of a Non-Aqueous Vanadium Acetylacetonate Prototype Redox Flow Battery: Examination of Separators and Capacity Decay," J. Electrochem. Soc., **162**(3), pp. A363–A372.
[63] Katinas, V., Gecevicius, G., and Marciukaitis, M., 2018, "An Investigation of Wind Power Density Distribution at Location With Low and High Wind Speeds Using Statistical Model," Appl. Energy, **218**, pp. 442–451.
[64] Binyu, X., Jiyun, Z., and Jinbin, L., 2013, "Modeling of an All-Vanadium Redox Flow Battery and Optimization of Flow Rates," 2013 IEEE Power Energy Society General Meeting, pp. 1–5.
[65] Darcy, H., 1803–1858, 1856, "Les fontaines publiques de la ville de Dijon: exposition et application des principes à suivre et des formules à employer dans les questions de distribution d'eau…/ par Henry Darcy,…," Distrib. Eau, p. 659.
[66] Carman, P. C., 1997, "Fluid Flow Through Granular Beds," Chem. Eng. Res. Des., **75**, pp. S32–S48.
[67] Deen, D., and William, M., 2012, *Analysis of Transport Phenomena*, Oxford University Press, NY.
[68] Forchheimer, P. H., 1901, "Wasserbewegung Durch Boden," Z. Acker-Pflanzenbau, **45**, pp. 1782–1788.
[69] Sobieski, W., and Trykozko, A., 2014, "Darcy's and Forchheimer's Laws in Practice. Part 1. The Experiment," Tech. Sci., **17**(4), pp. 321–335.
[70] Gostick, J. T., Fowler, M. W., Pritzker, M. D., Ioannidis, M. A., and Behra, L. M., 2006, "In-Plane and Through-Plane Gas Permeability of Carbon Fiber Electrode Backing Layers," J. Power Sources, **162**(1), pp. 228–238.
[71] Geertsma, J., 1974, "Estimating the Coefficient of Inertial Resistance in Fluid Flow Through Porous Media," Soc. Pet. Eng. J., **14**(5), pp. 445–450.
[72] Zeng, Z., and Grigg, R., 2006, "A Criterion for Non-Darcy Flow in Porous Media," Transp. Porous Media, **63**(1), pp. 57–69.
[73] Ma, H., and Ruth, D. W., 1993, "The Microscopic Analysis of High Forchheimer Number Flow in Porous Media," Transp. Porous Media, **13**(2), pp. 139–160.
[74] Feser, J. P., Prasad, A. K., and Advani, S. G., 2006, "Experimental Characterization of In-Plane Permeability of Gas Diffusion Layers," J. Power Sources, **162**(2), pp. 1226–1231.
[75] Rama, P., Liu, Y., Chen, R., Ostadi, H., Jiang, K., Gao, Y., Zhang, X., Brivio, D., and Grassini, P., 2011, "A Numerical Study of Structural Change and Anisotropic Permeability in Compressed Carbon Cloth Polymer Electrolyte Fuel Cell Gas Diffusion Layers," Fuel Cells, **11**(2), pp. 274–285.
[76] Ozgumus, T., Mobedi, M., and Ozkol, U., 2014, "Determination of Kozeny Constant Based on Porosity and Pore to Throat Size Ratio in Porous Medium With Rectangular Rods," Eng. Appl. Comput. Fluid Mech., **8**(2), pp. 308–318.
[77] Tomadakis, M. M., and Sotirchos, S. V., 1991, "Effective Kundsen Diffusivities in Structures of Randomly Overlapping Fibers," AIChE J., **37**(1), pp. 74–86.
[78] Tomadakis, M. M., and Sotirchos, S. V., 1993, "Effective Diffusivities and Conductivities of Random Dispersions of Nonoverlapping and Partially Overlapping Unidirectional Fibers," J. Chem. Phys., **99**(12), pp. 9820–9827.
[79] Tomadakis, M. M., and Sotirchos, S. V., 1993, "Ordinary and Transition Regime Diffusion in Random Fiber Structures," AIChE J., **39**(3), pp. 397–412.
[80] Tomadakis, M. M., and Robertson, T. J., 2005, "Viscous Permeability of Random Fiber Structures: Comparison of Electrical and Diffusional Estimates With Experimental and Analytical Results," J. Compos. Mater., **39**(2), pp. 163–188.
[81] Karakashov, B., Toutain, J., Achchaq, F., Legros, P., Fierro, V., and Celzard, A., 2019, "Permeability of Fibrous Carbon Materials," J. Mater. Sci., **54**(21), pp. 13537–13556.
[82] Bruggeman, D. A. G., 1935, "Berechnung Verschiedener Physikalischer Konstanten von Heterogenen Substanzen. I. Dielektrizitätskonstanten und Leitfähigkeiten der Mischkörper aus Isotropen Substanzen," Ann. Phys., **416**(7), pp. 636–664.
[83] van Brakel, J., and Heertjes, P. M., 1974, "Analysis of Diffusion in Macroporous Media in Terms of a Porosity, a Tortuosity and a Constrictivity Factor," Int. J. Heat Mass Transfer, **17**(9), pp. 1093–1103.
[84] Tjaden, B., Cooper, S. J., Brett, D. J., Kramer, D., and Shearing, P. R., 2016, "On the Origin and Application of the Bruggeman Correlation for Analysing Transport Phenomena in Electrochemical Systems," Curr. Opin. Chem. Eng., **12**, pp. 44–51.
[85] You, X., Ye, Q., and Cheng, P., 2017, "The Dependence of Mass Transfer Coefficient on the Electrolyte Velocity in Carbon Felt Electrodes: Determination and Validation," J. Electrochem. Soc., **164**(11), pp. E3386–E3394.
[86] Ma, X., Zhang, H., and Xing, F., 2011, "A Three-Dimensional Model for Negative Half Cell of the Vanadium Redox Flow Battery," Electrochim. Acta, **58**, pp. 238–246.
[87] Cooper, S. J., Bertei, A., Shearing, P. R., Kilner, J. A., and Brandon, N. P., 2016, "TauFactor: An Open-Source Application for Calculating Tortuosity Factors From Tomographic Data," SoftwareX, **5**, pp. 203–210.
[88] Carta, R., Palmas, S., Polcaro, A. M., and Tola, G., 1991, "Behaviour of a Carbon Felt Flow by Electrodes Part I: Mass Transfer Characteristics," J. Appl. Electrochem., **21**(9), pp. 793–798.
[89] Kinoshita, K., and Leach, S. C., 1982, "Mass-Transfer Study of Carbon Felt, Flow-Through Electrode," J. Electrochem. Soc., **129**(9), pp. 1993–1997.
[90] Schmal, D., Van Erkel, J, and Van Duin, P. J., 1986, "Mass Transfer at Carbon Fibre Electrodes," J. Appl. Electrochem., **16**(3), pp. 422–430.
[91] Newman, J., and Tiedemann, W., 1978, "Flow-Through Porous Electrodes," Adv. Electrochem. Electrochem. Eng., **11**, pp. 353–435.
[92] Recio, F. J., Herrasti, P., Vazquez, L., Ponce de León, C., and Walsh, F. C., 2013, "Mass Transfer to a Nanostructured Nickel Electrodeposit of High Surface Area in a Rectangular Flow Channel," Electrochim. Acta, **90**, pp. 507–513.
[93] Kok, M. D. R., Jervis, R., Tranter, T. G., Sadeghi, M. A., Brett, D. J. L., Shearing, P. R., and Gostick, J. T., 2019, "Mass Transfer in Fibrous Media With Varying Anisotropy for Flow Battery Electrodes: Direct Numerical Simulations with 3D X-Ray Computed Tomography," Chem. Eng. Sci., **196**, pp. 104–115.
[94] Moressi, M. B., and Fernández, H., 1994, "The Use of Ultramicroelectrodes for the Determination of Diffusion Coefficients," J. Electroanal. Chem., **369**(1–2), pp. 153–159.
[95] Bergner, B. J., Schürmann, A., Peppler, K., Garsuch, A., and Janek, J., 2014, "TEMPO: A Mobile Catalyst for Rechargeable Li-O_2 Batteries," J. Am. Chem. Soc., **136**(42), pp. 15054–15064.
[96] Nutting, J. E., Rafiee, M., and Stahl, S. S., 2018, "Tetramethylpiperidine N-Oxyl (TEMPO), Phthalimide N-Oxyl (PINO), and Related N-Oxyl Species: Electrochemical Properties and Their Use in Electrocatalytic Reactions," Chem. Rev., **118**(9), pp. 4834–4885.
[97] Saha, K. C., and Mandal, P. C., 2002, "Electrochemical Oxidation and Reduction of Nitroxides: A Cyclic Voltammetric and Simulation Study," Indian J. Chem., **41A**(11), pp. 2231–2237.
[98] Yen, H. T. H., 2014, "Electrochemical Investigations of the Diffusion Coefficients and the Heterogeneous Electron Transfer Rates of Organic Redox Couples Measured in Ionic Liquids," Dissertation, Technischen Universität Gra.
[99] Aris, R., 1989, *Elementary Chemical Reactor Analysis*, Dover, New York.
[100] Green, L. J., and Duwez, P., 1951, "Fluid Flow Through Porous Media," J Appl. Mech, **18**(1), pp. 39–45.
[101] Berg, C. F., 2014, "Permeability Description by Characteristic Length, Tortuosity, Constriction and Porosity," Transp. Porous Media, **103**(3), pp. 381–400.